Magnetization dynamics of soft films with thickness-dependent anisotropy

Vincent Dubuget
Laboratoire d'Electrodynamique des Matériaux Avancés, UMR 6157 CNRS, Université François Rabelais, Parc de Grandmont, F-37200 Tours, France and Commissariat à l'Energie Atomique Le Ripault, BP 16, F-37260 Monts, France

André Thiaville
Laboratoire de Physique des Solides, CNRS, Université Paris-Sud, F-91405 Orsay Cedex, France

François Duverger, Sébastien Dubourg, Olivier Acher, and Anne-Lise Adenot-Engelvin
Commissariat à l'Energie Atomique Le Ripault, BP 16, F-37260 Monts, France

(Received 16 March 2009; revised manuscript received 9 September 2009; published 13 October 2009)

The static and dynamic magnetic properties of samples consisting of two soft magnetic layers with in-plane easy axes at right angles are studied by micromagnetics and experiments. A one-dimensional micromagnetic model is developed, and solved quasianalytically for statics and dynamics. In particular, it is shown that the magnetic permeability arises from a set of eigenmodes, each with a macrospin (or gyromagnetic) response, that are excited differently depending on ac field orientation. Experiments (magnetization curves, permeability under field and in several directions) on cobalt-based amorphous alloy bilayers are well reproduced by the model with a single set of parameters. Such samples are therefore model one-dimensional nonuniform magnetic systems, simple yet with a rich behavior, for statics and dynamics.

DOI: 10.1103/PhysRevB.80.134412 PACS number(s): 75.60.Ch, 75.70.Ak, 76.50.+g, 41.20.Jb

I. INTRODUCTION

Magnetization fast dynamics, by precession around the total magnetic field, is an old[1,2] but still vivid subject.[3–5] In nanostructures, it has lead to a very efficient magnetization switching strategy, called precessional switching.[6] Precessional dynamics is rich and complex, as the total field is the sum of the applied field and the anisotropy field, the latter changing as magnetization rotates. But this can be analytically handled,[7,8] and the same tools can also be applied to magnetization dynamics under spin transfer torque.[9]

One of the main assumptions underlying this analytical modeling is the macrospin approximation, according to which the sample moments stay always parallel during their motion. In the frequency domain, the macrospin model translates into the existence of a single resonance frequency with a lineshape fixed by energy relaxation (damping), a dynamic analog of the Stoner-Wohlfarth model sometimes termed the gyromagnetic model. When the macrospin approximation does not hold, the complexity of the dynamics increases greatly, and several resonance peaks can be expected.

In the case of a soft magnetic thin film consisting of grains with dipolar and exchange coupling, spin wave hamiltonian diagonalization has indeed shown resonance peak broadening and splitting, depending on the size of the grains.[10] Such grain to grain fluctuations give rise to static magnetization patterns with characteristic local deviations, called the ripple structure.[11] Moreover, when going down to patterned strips or nanostructures where dipolar fields are nonuniform, modes with well separated frequencies have been observed even under high fields.[12]

In this work, we investigate magnetization dynamics in amorphous films, where no ripple is expected. It has been shown earlier that, as the thickness of the film increases, the permeability spectra differ more and more from the gyromagnetic model.[13–15] As a first interpretation, it was noticed that above the so-called critical thickness, stripe domains form due to the presence of a (small) growth-induced perpendicular anisotropy.[11] The micromagnetic calculation of magnetization dynamics in such a structure indeed showed several peaks, related to different regions, that reproduced the experimental permeability spectra.[16,17] But, on the other hand, experiments show that, even without stripe domains, the spectra display wider peaks with sometimes subpeaks.[13] Magnetic domains at the sample edges have been shown to lead to some low frequency subpeaks,[18] but cannot account for higher frequency subpeaks. An inhomogeneity in the film thickness is one possible cause of this behavior. For example, stress can accumulate during film growth, leading to a variation of anisotropy across the thickness (through magnetostriction).

In order to systematically investigate the effect of such an anisotropy variation, we will consider in this paper two-layer films with different magnetic anisotropies in each layer. Section II is devoted to the calculation of this case, first for statics and then for dynamics. We propose to call such kind of magnetic structure a one-dimensional (1D) spiral. A semianalytic solution for the 1D spiral is derived, that for statics goes beyond previous work by establishing the boundaries in parameter space of the strictly uniform magnetization situations. In addition, an extensive description of the magnetization dynamics for this 1D nonuniform state is obtained by the introduction of a complete set of eigenmodes. Section III presents the results of experiments performed with specially fabricated two-layer samples, both in static and dynamic conditions (permeability spectra). Using a single set of parameters, the comparison between model and experiments is rather good, and the spectra as well as their evolution under static field bear some similarity to measurements on single layer samples. Thus, variation of anisotropy across the sample thickness is a simple yet sufficiently rich case of

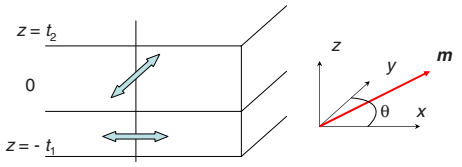

FIG. 1. (Color online) Geometry and definitions for a sample constituted of two layers with crossed anisotropies. The angle $\theta(z,t)$ defines the orientation of the magnetization in the xy plane. The in-plane angles of the static and dynamic magnetic fields are denoted by θ_H and θ_h, respectively.

magnetization nonuniformity, that can apply to measurements on magnetic "thick" films.

II. MODEL SYSTEM OF TWO LAYERS WITH CROSSED ANISOTROPIES

A. Definitions

In this paper, we study in depth the case of a thin film sample, magnetically soft with in-plane anisotropy. As source of nonuniformity, it is assumed that only the anisotropy changes across the sample thickness. The simplest such case is afforded by a two-layer film (Fig. 1), the bottom layer (thickness t_1) having an easy axis along the x direction ($\theta_{K1}=0$) with anisotropy constant K_1, whereas the top layer (thickness t_2) has an easy axis along the orthogonal direction ($y, \theta_{K2}=\pi/2$) with anisotropy constant K_2. The anisotropy imbalance between the two layers will be expressed by the ratio $k_1=K_1/(K_1+K_2)$ and $k_2=K_2/(K_1+K_2)=1-k_1$. This may be called the crossed anisotropies situation. All other magnetic parameters, such as the magnetization M_s and the exchange energy constant A, are constant.

The magnetic softness of the sample is expressed by the conditions $H_{K1}, H_{K2} \ll M_s$, where the anisotropy field in each layer is defined by $H_{Ki}=2K_i/(\mu_0 M_s)$ $(i=1,2)$. We will study here the low field processes, where the static applied field H_0 is also much lower than the magnetization M_s, and applied in the sample plane (angle θ_H).

B. Statics

In static conditions, as both easy axes and the applied field are in the xy sample plane, magnetization is also confined to that plane. It can therefore be described by one angle, θ (Fig. 1), a function of the position z to be determined. This angle is pulled toward orthogonal directions in each layer, a tendency counterbalanced by the exchange interaction. Micromagnetics allows treating this problem analytically,[19] as a more complex version of the calculation of the Bloch wall profile. The total micromagnetic energy per unit surface, and in the presence of an applied field, reads

$$E = \int_{-t_1}^{t_2} \left[A\left(\frac{d\theta}{dz}\right)^2 + K \sin^2(\theta - \theta_K) - \mu_0 M_s H_0 \cos(\theta - \theta_H) \right] dz, \quad (1)$$

where K and θ_K are step functions of z [$K(z)=K_1$ and $\theta_K=0$ for $-t_1<z<0$; $K(z)=K_2$ and $\theta_K=\pi/2$ for $0<z<t_2$]. From the competition of exchange and anisotropy energies, two lengths can be defined by $\Delta_i=\sqrt{A/K_i}$ (the Bloch wall width parameter in each layer). It is important to remark that, as $K_i \ll \mu_0 M_s^2$, these lengths are large, $\approx$100 nm with the parameters considered.

The Euler-Lagrange equation for E to be an extremum is best written separately in each layer

$$-2A\frac{d^2\theta}{dz^2} + K_1 \sin 2\theta + \mu_0 M_s H_0 \sin(\theta - \theta_H) = 0$$

for

$$-t_1 < z < 0;$$

$$-2A\frac{d^2\theta}{dz^2} - K_2 \sin 2\theta + \mu_0 M_s H_0 \sin(\theta - \theta_H) = 0$$

for

$$0 < z < t_2. \quad (2)$$

The boundary conditions are free at the outer surfaces (we assume free surfaces for all this paper, for simplicity, although the methods could be extended to surfaces with nonzero pinning)

$$\frac{d\theta}{dz} = 0 \quad \text{with } z = -t_1, t_2; \quad (3)$$

and express continuity at the internal interface

$$\theta, \ \frac{d\theta}{dz} \text{ continuous at } z = 0. \quad (4)$$

As for the Bloch wall profile calculation, the Euler-Lagrange equation possesses a first integral

$$-A\left(\frac{d\theta}{dz}\right)^2 + K_1 \sin^2\theta - \mu_0 M_s H_0 \cos(\theta - \theta_H) = C^{st}$$
$$= K_1 \sin^2\theta_1 - \mu_0 M_s H_0 \cos(\theta_1 - \theta_H) \quad \text{for } -t_1 < z < 0, \quad (5)$$

where $\theta_1 \equiv \theta(z=-t_1)$ was inserted and the outer boundary condition (3) was used. Similarly, for the second layer, one gets

$$-A\left(\frac{d\theta}{dz}\right)^2 + K_2 \cos^2\theta - \mu_0 M_s H_0 \cos(\theta - \theta_H)$$
$$= K_2 \cos^2\theta_2 - \mu_0 M_s H_0 \cos(\theta_2 - \theta_H) \quad (6)$$

for

$$0 < z < t_2,$$

with $\theta_2 \equiv \theta(z=t_2)$. From these first integrals, by separation of variables, z can be expressed as an (elliptic) function of θ, with θ_1 and θ_2 as parameters. These two parameters are determined by the two continuity conditions (4) at $z=0$. This completes formally the analytical solution of the static problem. Of course, the problem considered here, as well as more complex variants where more parameters vary and in a more

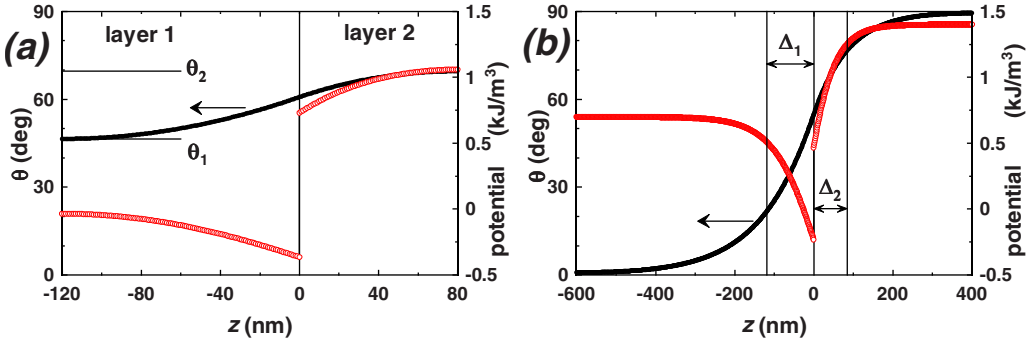

FIG. 2. (Color online) Profile of the magnetization angle across the sample thickness for the (a) thin sample and the (b) thick sample. The right scale depicts in addition the "potential" associated to the static solution, a quantity relevant for the calculation of the magnetization oscillation modes.

complex manner, can also be solved numerically with little effort (see for example Ref. 20). However, for the simple situation considered here, the analytic solution exists, allows for a general understanding at once, and is well adapted to study the limiting cases, as shown later.

1. Zero field case

In order to solve completely the problem, we define auxiliary angles: in the first layer $-t_1<z<0$ we write $\cos\theta=\cos\theta_1\sin\psi$ so that $\psi(-t_1)=\pi/2$ and $\psi(0)\equiv\psi_0$; whereas in the second layer $0<z<t_2$ the definition is $\sin\theta=\sin\theta_2\sin\phi$ so that $\phi(t_2)=\pi/2$ and $\phi(0)\equiv\phi_0$. The continuity conditions at $z=0$ Eq. (4) provide the values of ψ_0 and ϕ_0, once θ_1 and θ_2 are known, as

$$\sin^2\psi_0=k_1+k_2\frac{\cos^2\theta_2}{\cos^2\theta_1},$$

$$\sin^2\phi_0=k_2+k_1\frac{\sin^2\theta_1}{\sin^2\theta_2}. \tag{7}$$

The values of θ_1 and θ_2 are determined by solving the following implicit system:

$$\frac{t_1}{\Delta_1}=\int_{\psi_0}^{\pi/2}\frac{d\alpha}{\sqrt{1-\cos^2\theta_1\sin^2\alpha}},$$

$$\frac{t_2}{\Delta_2}=\int_{\phi_0}^{\pi/2}\frac{d\alpha}{\sqrt{1-\sin^2\theta_2\sin^2\alpha}}. \tag{8}$$

Throughout this section, numerical values will be shown for a material having $M_s=700$ kA/m, $A=1\times10^{-11}$ J/m, $H_{K1}=20$ Oe ($\mu_0H_{K1}=2$ mT, $K_1=700$ J/m^3) and $H_{K2}=40$ Oe ($\mu_0H_{K2}=4$ mT, $K_2=1400$ J/m^3), $\gamma=2.21\times10^5$ m/(A.s) and $\alpha=0.02$ for dynamics. These parameters are representative of the soft cobalt-based alloys used in the experiments described in Sec. III. Numerically, the Bloch wall width parameters amount here to $\Delta_1=119.52$ nm and $\Delta_2=84.52$ nm, and $k_1=1/3$. Two "samples" will be considered, one "thin" with $t_1=120$ nm and $t_2=80$ nm (so that $t_1/\Delta_1, t_2/\Delta_2\simeq1$), and the other "thick" with $t_1=600$ nm and $t_2=400$ nm. The results shown below were obtained by solving numerically the system (8) through an iterative adjustment of θ_1 and θ_2. For this, we start from a guess for θ_1 and θ_2, compute ϕ_0 and ψ_0 from Eq. (7), evaluate numerically the integrals on the rhs of Eq. (8) and compare them to the lhs; the values of θ_1 and θ_2 are then iteratively modified according to a Newton procedure until Eq. (8) is satisfied to a given precision (typically 10^{-4}). Once these values are found, the $\theta(z)$ profiles are obtained by replacing, in Eq. (8), ψ_0 by values ψ between 0 and ψ_0 and computing the associated depths $(-z)$ between 0 and t_1 (and similarly for the profile in the second layer).

Figure 2 shows the $\theta(z)$ profiles for the two films. For the thin sample [Fig. 2(a)] one has $\theta_1=46.46°$ and $\theta_2=69.56°$ so that the variation of θ across the thickness is moderate, as the thicknesses are comparable to the characteristic lengths Δ_i (we give precise values as the solution depends sensitively on these angles in that case, see Fig. 3). For the thick film [Fig. 2(b)], the end values are much closer to the easy axes ($\theta_1=0.78°$, $\theta_2=89.36°$), as expected. The angle of the average moment of the sample is $\theta_M=57.46°$ and 39.11°, respectively. An alternative definition of this angle, through the rms averages of m_x and m_y (Ref. 21) (see also the Appendix on this subject), gives rather close values: 56.89° and 37.65°, respectively.

In order to depict all solutions of the problem at once, a "phase diagram" is constructed in Fig. 3. From the Eqs. (7) and (8), it results that the problem is fully determined by the nondimensional quantities t_1/Δ_1, t_2/Δ_2 and k_1. This phase space consists of three regions: a (largest) region with a nonuniform θ, bounded by two regions, one in which $\theta(z)=0$ everywhere and another one where $\theta(z)=\pi/2$ everywhere. By expansion around the $\theta=0$ solution of the equations, it is possible to obtain the definition of the first region (magnetization uniformly along the x direction) as

$$\frac{t_1}{\Delta_1}\geq\ln[\sqrt{k_2(a^2-1)}+\sqrt{1+k_2(a^2-1)}],$$

$$\frac{t_2}{\Delta_2}\leq\mathrm{A}\cos\sqrt{k_2+\frac{k_1}{a^2}}, \tag{9}$$

where the parameter $a>1$ is the ratio θ_2/θ_1 of the deviations. The boundary of the $\theta(z)=\pi/2$ region is given by the same equation where the roles of 1 and 2 are exchanged. At

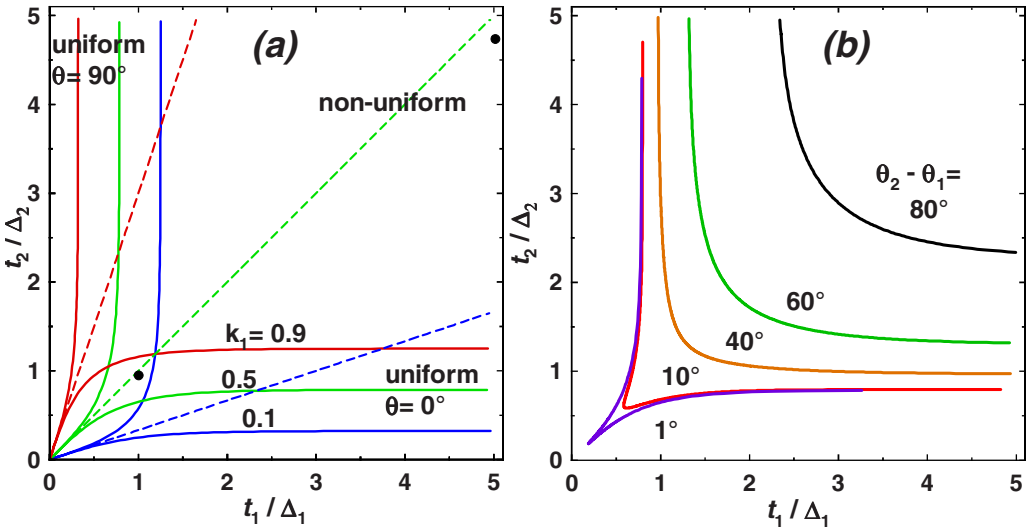

FIG. 3. (Color online) Representation, in the plane spanned by t_1/Δ_1 and t_2/Δ_2, of the different phases of the solution, with k_1 as a parameter. The three phases are: uniform along x, uniform along y and, in between, nonuniform. The straight lines through the origin show the one spin solution of the problem. The dots indicate the two cases considered throughout this section. For panel (a) three values of k_1 are shown. Panel (b) applies to $k_1=1/2$ only and plots several contour lines for the difference $\theta_2-\theta_1$.

the origin, both boundaries have the same tangent, namely,

$$\frac{t_2/\Delta_2}{t_1/\Delta_1}=\sqrt{\frac{k_1}{k_2}} \quad i.e. \quad t_1K_1=t_2K_2. \tag{10}$$

Therefore, this line is also the solution of the problem in the single spin approximation, where the nonuniform region is absent by construction. These results bear some similarity with the solution for the magnetization profile in a thin film with perpendicular surface anisotropy.[22]

In Fig. 3(a), the boundaries of the uniform regions are drawn for the three cases $k_1=0.1$, 0.5 and 0.9. The dots representing the thick and thin films (with $k_1=1/3$) are also indicated. In Fig. 3(b), specialized to the case $k_1=0.5$, some lines with constant difference $\theta_2-\theta_1$ are drawn.

2. Nonzero field

The solution found in zero field is obviously fourfold degenerate, with one variant in each quadrant of the plane. This degeneracy is lifted by an applied field, fully for a nonspecial angle (θ_H not a multiple of $\pi/2$). As we will compare later to measurements on macroscopic samples, only the case where the field is applied in the quadrant of the solution will be relevant. Indeed, domain wall motion eliminates the other variants as soon as the field exceeds coercivity, typically $\mu_0 H_c=0.2$ mT (2 Oe, 160 A/m) for the samples experimentally investigated in this study. Of course, from a mathematical point of view, the magnetization curves can be followed in the unstable regime, down to the end of metastability.

3. Analytical results

Some results concerning the boundaries of the uniform regions, under field, can be obtained analytically. First, the $\theta=0$ uniform region exists only when $\theta_H=0$ (and the $\theta=\pi/2$ region exists only when $\theta_H=\pi/2$). Indeed, an oblique field causes a rotation of magnetization, which is nonuniform as the restoring forces are different in each layer. The boundary of the $\theta=0$ uniform region under field is obtained, similarly to the zero field case, as

$$\frac{t_1}{\Delta_1}\geq\frac{1}{\sqrt{1+h_1}}\ln\left[\sqrt{1+(k_2-k_1h_1)(a^2-1)}+\sqrt{(k_2-k_1h_1)(a^2-1)}\right],$$

$$\frac{t_2}{\Delta_2}\leq\frac{1}{\sqrt{1-h_2}}\mathrm{A}\cos\left[\sqrt{\frac{1}{a^2}+(k_2-k_1h_1)\left(1-\frac{1}{a^2}\right)}\right], \tag{11}$$

where $h_1=H_x/H_{K1}$ and $h_2=H_x/H_{K2}=h_1(k_1/k_2)$ are the two reduced forms of the applied field, in each layer. Comparing to the zero field case (9), we can remark that the lower limit for t_1 decreases, and the upper limit for t_2 increases when the field is larger, as expected. Strangely at first sight, the formula above applies only to the case $k_2-k_1h_1>0$, i.e., $h_2<1$. This is no surprise however, as for $h_2>1$ the sample is saturated along the x axis whatever the thickness, as the field for layer 2 is in the hard direction and larger than the anisotropy field.

4. Magnetization curves

The calculated magnetization curves (projection of the total moment of the sample along the field direction) for the thin sample are shown in Fig. 4(a), for fields oriented along the x axis, the y axis and along the direction of the average magnetization. The thick sample case is illustrated, similarly, in Fig. 4(b). These curves were obtained by a numerical solution of the problem.

In the thick sample case, the saturation field in the x direction is a little smaller than H_{K2}, and similarly for the y

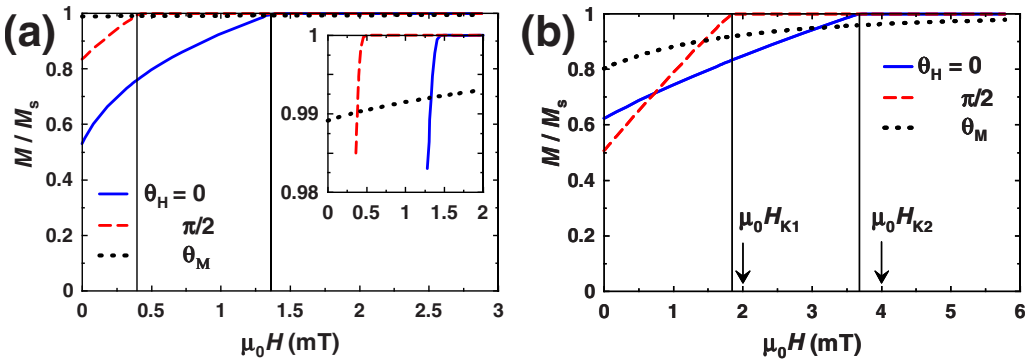

FIG. 4. (Color online) Magnetization curves (stable branch only) for (a) the thin sample and (b) the thick sample. For each case, the field is applied in the x and y directions, as well as along the average magnetization orientation in zero field. The vertical lines mark the saturation fields computed from the analytical formulas giving the boundaries of the uniform regions. Note the different horizontal scales. In the thin sample case, the inset shows the different approaches to saturation.

direction and H_{K1}. The equality should be perfect if there were no exchange coupling between both parts of the film or, equivalently, if they were much thicker than the corresponding domain wall widths. In such a case, the curves would be hard axis curves of the Stoner-Wohlfarth model, hence perfectly linear and start from initial values given by t_2/t (t_1/t). This is indeed not far from the calculation results. But in fact, we already have an analytic calculation of the saturation field in the x direction by the solution of Eq. (11) in terms of h_1 and the parameter a (and similarly for the y saturation field). These values are indicated in Fig. 4. On the other hand, the curve for a field applied along the average magnetization shows a progressive saturation, as the field is applied in a nonspecial direction for both layers.

In comparison, for the thin sample [Fig. 4(a)], the calculated behavior differs strongly from a model with no exchange between both layers: more curvature is present and the apparent saturation fields are much reduced (but still agree with the analytical relation). These small apparent anisotropy fields are close to the limiting value obtained in the macrospin model, namely $\mu_0 H_K = 0.4$ mT here with an easy axis along y.

In order to show how much the saturation fields can be affected by the magnetization nonuniformity in the sample, the curves of constant saturation field in the x and y directions were constructed from the analytical relations (11). They are displayed in Fig. 5, in the $(t_1/\Delta_1, t_2/\Delta_2)$ plane. At low thickness, the curves are straight lines that correspond to the macrospin solution, which is, in the case of an x field

$$\frac{t_2/\Delta_2}{t_1/\Delta_1} = \frac{1+h_1}{1-h_2}\sqrt{\frac{k_1}{k_2}}. \tag{12}$$

However, still for an x field for the sake of definiteness, as soon as $t_1/\Delta_1 > 1$, roughly, the limiting t_2 value becomes independent of t_1. More precisely, the figure shows that the departure from the macrospin model begins at $t_1/\Delta_1 \approx 0.5$.

Some profiles of angle versus depth corresponding to these data are shown in Fig. 6, for the case of the thick sample. The evolution toward $\theta = 0$ (for $\theta_H = 0$) and toward $\theta = \pi/2$ (for $\theta_H = \pi/2$) is illustrated in Fig. 6(a), whereas Fig. 6(b) shows how the profiles straighten for a field oriented along the average zero field magnetization.

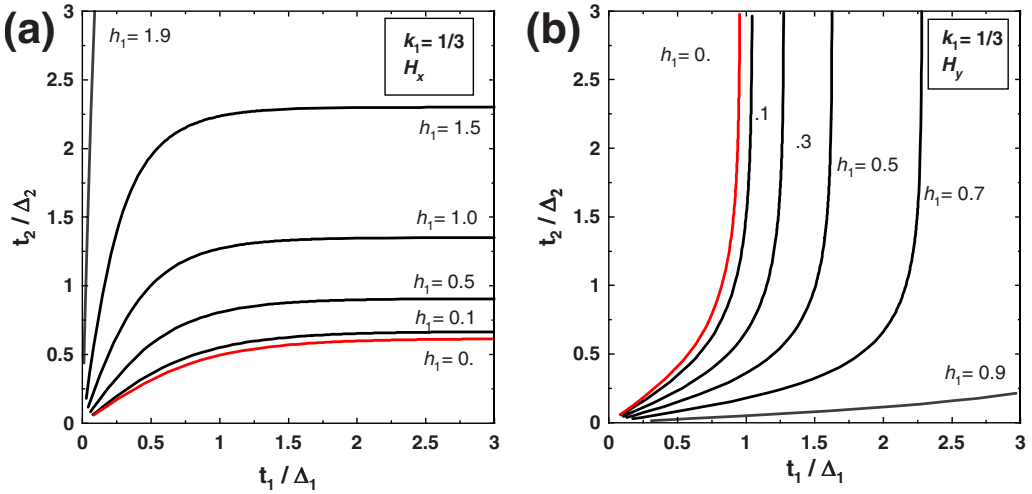

FIG. 5. (Color online) Curves of constant saturation field, for a field applied in the (a) x direction, and in (b) the y direction, in the case where $k_1 = 1/3$. Field values are given by $h_1 = H/H_{K1}$. In the x field case, saturation is reached whatever the thicknesses at $H_x = H_{K2}$, i.e., $h_1 = 2$ here. In the y field case, this becomes $H_y = H_{K1}$, thus $h_1 = 1$. The slopes at the origin in (a) conform to Eq. (12).

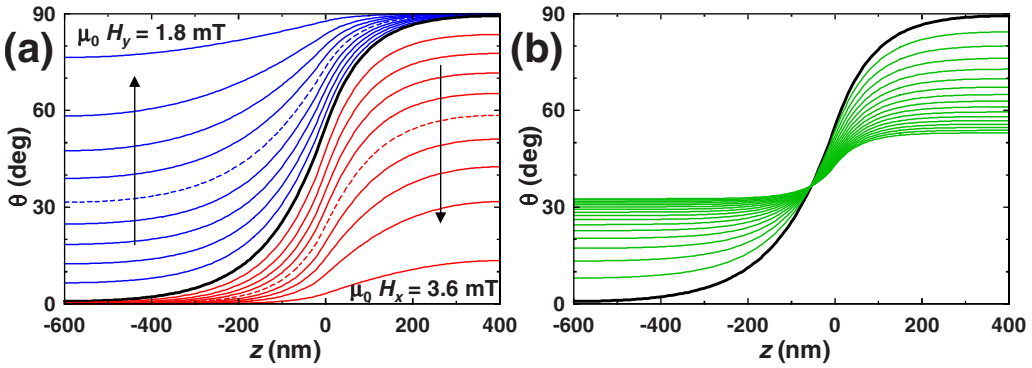

FIG. 6. (Color online) Profiles of the magnetization angle across the sample thickness for the thick sample, under field (the thick black curve is the zero field profile). Graph (a) contains the profiles for a field in the x orientation (red lines below the zero field profile, from 0.4 to 3.6 mT with a step of 0.4 mT) and in the y orientation (blue lines above the zero field profile, from 0.2 to 1.8 mT with a step of 0.2 mT). Panel (b) is for a field along the direction of the average magnetization in zero field (from 0.5 to 8 mT with a step of 0.5 mT).

Thus, we have now a complete description of the statics of this model film with a two layers structure. Except for special cases, the magnetization of the sample is not uniform across the thickness, with a structure similar to a finite angle domain wall: the 1D spiral. The width of this structure is, because soft materials are considered, of the order of 100 nm typically.

C. Linear dynamics without skin effect

We now turn to the calculation of the magnetization dynamics, under an infinitesimally small ac field, of this nonuniform structure. Specifically, we want to evaluate the dynamic magnetic susceptibility of such a sample, in the frequency range that encompasses ferromagnetic resonance, from the MHz to a few tens of GHz, typically.

1. Hypotheses

As the sample is supposed to be excited by a uniform ac field, only uniform modes in the x-y plane will be calculated. This leaves aside all spin wave modes propagating in the sample plane. Moreover, in the permeability measurements described later that average over a large sample surface, such modes should not be visible. The time dependent magnetization will be written as

$$\vec{m} = (\cos\,\theta\cos\,\upsilon, \sin\,\theta\cos\,\upsilon, \sin\,\upsilon) \tag{13}$$

with $\theta(z,t)=\theta_0(z)+u(z,t)$ where $\theta_0(z)$ denotes the static solution. The deviations u (in-plane rotation angle) and υ (out-of-plane rotation angle) are infinitesimally small in the linear regime: $|u(z,t)|$, $|\upsilon(z,t)| \ll 1$.

The energy of the sample under a time independent field $\vec{H}_0$ (angle θ_H and magnitude H_0) and an in-plane ac field $[h_x(t), h_y(t), 0]$ reads now

$$E = \int_{-t_1}^{t_2} \left\{ A\left[\cos^2\upsilon\left(\frac{d\theta}{dz}\right)^2 + \left(\frac{d\upsilon}{dz}\right)^2\right] - K\cos^2(\theta-\theta_K)\cos^2\upsilon + \frac{\mu_0 M_s^2}{2}\sin^2\upsilon - \mu_0 M_s H_0 \cos\upsilon\cos(\theta-\theta_H) - \mu_0 M_s \cos\upsilon(h_x\cos\,\theta + h_y\sin\,\theta)\right\} dz. \tag{14}$$

Note that, as the magnetization varies only in the z direction, the magnetostatic energy density is very simple. The dynamics of the magnetization under the Landau-Lifshitz-Gilbert (LLG) equation requires the calculation of the effective field, defined by the energy differential

$$dE = -\mu_0 M_s \int_{-t_1}^{t_2} (H_u du + H_\upsilon d\upsilon) dz. \tag{15}$$

2. Case with no static field

In the limit of vanishing u, υ, h_x, and h_y (all of the same order) we have to first order

$$H_u = \frac{1}{\mu_0 M_s}\left[2A\frac{d^2u}{dz^2} - 2uK\cos 2(\theta_0-\theta_K) + \mu_0 M_s(-h_x\sin\,\theta_0 + h_y\cos\,\theta_0)\right],$$

$$H_\upsilon = \frac{1}{\mu_0 M_s}\left\{2A\frac{d^2\upsilon}{dz^2} + 2\upsilon\left[A\left(\frac{d\theta_0}{dz}\right)^2 - K\cos^2(\theta_0-\theta_K) - \frac{\mu_0 M_s^2}{2}\right]\right\}. \tag{16}$$

The LLG equation is then simply (with $\gamma_0=\mu_0|\gamma|$, γ being the gyromagnetic ratio)

$$\frac{du}{dt} = \gamma_0 H_\upsilon - \alpha\frac{d\upsilon}{dt},$$

$$\frac{d\upsilon}{dt} = -\gamma_0 H_u + \alpha\frac{du}{dt}. \tag{17}$$

This linear system [from Eq. (16)] can be solved in the harmonic decomposition. For that, we define

$$h_x \equiv Xe^{-i\omega t}, \quad h_y \equiv Ye^{-i\omega t}, \quad u(z,t) \equiv U(z)e^{-i\omega t},$$

$$\upsilon(z,t) \equiv V(z)e^{-i\omega t}. \tag{18}$$

We first look for a solution of the problem in the quasistatic approximation, where electromagnetic effects, that lead

to eddy currents and limit the external ac field penetration in the sample thickness by the skin depth effect, can be neglected. In that case, X and Y do not depend on z, and are given by the incoming field. The LLG equation in terms of the functions $U(z)$ and $V(z)$ is linear, with a source term given by the applied ac field. However, the linear operators acting on U and V are differential. The operator contained in H_u is the same as the hamiltonian of a 1D Schrödinger equation, with a kinetic term and a potential term. Therefore, it can be diagonalized by solving the eigenvalue equation

$$-2A\frac{d^2U}{dz^2}+2K\cos 2(\theta_0-\theta_K)U=\mu_0M_s^2\lambda U, \tag{19}$$

where θ_0, θ_K, and K depend on z (the latter two being step functions). The resulting potentials have been plotted in Fig. 2 for the two cases considered in this section. The potential goes to constant values at the sample boundaries (different in both layers when their anisotropies differ), and has a dip in the vicinity of the interface, with a jump at the interface in this simplest model. By this procedure, a series of eigenfunctions $U_n(z)$ corresponding to eigenvalues λ_n will be found (note that, with this definition, λ_n has no dimensions). From the general properties of the Schrödinger equation, we know that the eigenfunctions are orthogonal

$$\int_{-t_1}^{t_2}U_m(z)U_n(z)dz=(t_1+t_2)\delta_{mn}, \tag{20}$$

and that they form a complete basis for the functions in the interval $[-t_1,t_2]$. Thus, without loss of generality, we can expand

$$U(z)=\Sigma_{n=1}^{\infty}a_nU_n(z). \tag{21}$$

Another operator is contained in H_v, also of the Schrödinger type, but with a different potential that reads $\mu_0M_s^2+2K\cos^2(\theta_0-\theta_K)-2A(d\theta_0/dz)^2$ instead of $2K\cos 2(\theta_0-\theta_K)$. Therefore its eigenfunctions are different. However, we remark that this second potential is dominated by the large value $\mu_0M_s^2$: the anisotropy is small and the characteristic scale for the variation of θ_0 is large compared to the exchange length $[\Delta_i\gg\Lambda=\sqrt{2A/(\mu_0M_s^2)}]$. Thus, in an approximation valid for the modes with the lowest frequencies, we can replace this operator by the constant $\mu_0M_s^2$. This allows using the eigenfunctions of the operator on U to solve the full problem. Developing the other variables on the eigenmodes $U_n(z)$

$$V(z)=\Sigma_nb_nU_n(z), \tag{22}$$

$$X\sin\theta_0-Y\cos\theta_0=\Sigma_nh_nU_n(z), \tag{23}$$

the LLG equation projected on the eigenmodes reads

$$-i\omega a_n=-\gamma_0M_sb_n+\alpha i\omega b_n,$$

$$-i\omega b_n=\gamma_0M_s\lambda_na_n-\alpha i\omega a_n+\gamma_0h_n, \tag{24}$$

whose solution is

$$a_n=\gamma_0h_n\frac{\gamma_0M_s-\alpha i\omega}{\omega^2(1+\alpha^2)+\alpha i\omega\gamma_0M_s(1+\lambda_n)-(\gamma_0M_s)^2\lambda_n}, \tag{25}$$

$$b_n=\frac{i\omega}{\gamma_0M_s-\alpha i\omega}a_n. \tag{26}$$

This solution is the same as that of a thin film sample described in the macrospin approximation with an anisotropy in the plane (anisotropy field λM_s) and a perpendicular magnetostatic shape anisotropy (anisotropy field M_s). The resonance frequency of mode n is

$$\omega_n=\gamma_0M_s\sqrt{\frac{\lambda_n}{1+\alpha^2}}\approx\gamma_0M_s\sqrt{\lambda_n}. \tag{27}$$

For the calculation of the susceptibility, the magnetization expanded to first order reads

$$\vec{m}(z,t)=\vec{m}_0(z)+e^{-i\omega t}\Sigma_n\{U_n(z)\times[-a_n(\omega)\sin\theta_0(z),a_n(\omega)\cos\theta_0(z),b_n(\omega)]\}. \tag{28}$$

The response has to be averaged over the sample thickness (in the quasistatic approximation) and projected along the applied ac field orientation in order to get the longitudinal susceptibility. This results into

$$\chi=\gamma_0M_s\Sigma_np_n\frac{\gamma_0M_s-\alpha i\omega}{\omega^2(1+\alpha^2)+\alpha i\omega\gamma_0M_s(1+\lambda_n)-(\gamma_0M_s)^2\lambda_n}=\mu-1, \tag{29}$$

where μ is the magnetic permeability. The factor $p_n=(h_n/H)^2$ is the weight of mode n in the spectrum, given by

$$\frac{h_n}{H}=-\frac{\int\sin(\theta_0(z)-\theta_h)U_n(z)dz}{t_1+t_2}, \tag{30}$$

where the ac field components X and Y are $X=H\cos\theta_h$ and $Y=H\sin\theta_h$. This means that the susceptibility in the nonuniform ground state is the sum of macrospinlike susceptibility curves, one for each mode n, with a weight that depends on the mode z profile and on the angle θ_h of the ac field.

The profiles of the first modes are shown in Fig. 7 for the thin sample [Fig. 7(a)] and the thick sample [Fig. 7(b)]. One observes, for the low index modes ($n<2$ for the thin sample, but $n<5$ for the thick sample), the influence of the shape of the potential (it was plotted in Fig. 2) on the mode profile. For higher indices, the influence of the potential shape disappears as the mode energy increases, and the mode tends to a sine wave as expected for a dominant kinetic term. Such modes are well known as (exchange dominated) perpendicular standing spin waves.[3]

The eigenvalues λ_n are plotted in Fig. 8 as a function of the index n, for both samples. At high index, the dominance of the exchange term leads to expect a variation according to

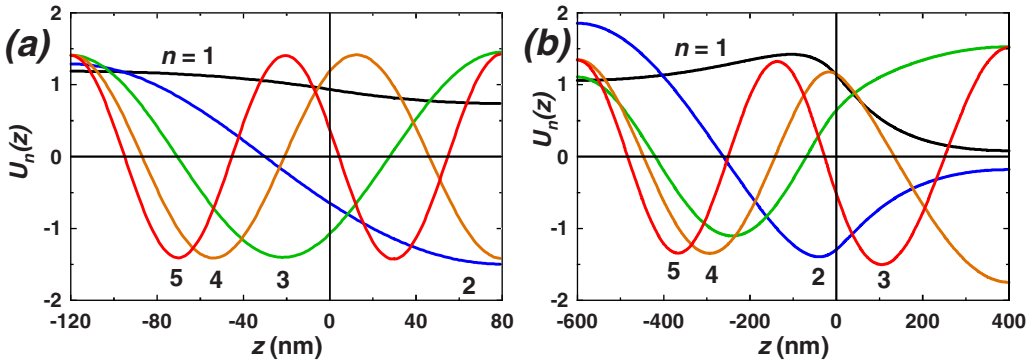

FIG. 7. (Color online) Profiles of the low-lying modes computed by numerical solution of the Schrödinger Eq. (19) with the potentials plotted in Fig. 2 for the (a) thin sample and (b) the thick sample. The modes are normalized according to Eq. (20). A mode of index n has $n-1$ zeroes.

$$\lambda_n \simeq C + \left(\frac{n\pi\Lambda}{t_1+t_2}\right)^2, \tag{31}$$

where C is the average value of the potential, in units of the magnetostatic energy density $\mu_0 M_s^2$. Thus, the mode resonance frequency should increase linearly with n at large indices. This is quantitatively verified in Fig. 8. In addition, Eq. (31) and Fig. 8 show that $\lambda \ll 1$ for the low mode indices, justifying the approximation made.

The frequency-dependent permeabilities calculated for the two samples are shown in Figs. 9 and 10, respectively (as the imaginary part is displayed, this is the same as the susceptibility). For each sample, different orientations of the ac field are shown: along x (a), along y (b), along the average magnetization (angle θ_M) (c) and orthogonal to this angle (d). From Eq. (29), it is easy to see that each mode contributes by p_n/λ_n to the initial susceptibility $\chi(\omega=0)$, and has an absorption maximum $\mu''_{max,n} \approx p_n/(\alpha\sqrt{\lambda_n})$. The weights vary as the field orientation changes (see Table I), so that the spectral shape of the susceptibility changes also.

In the case of the thin sample, the spectra appear to be very simple, with a single peak at a fixed frequency, except when the ac field is along the average magnetization. Moreover, the ratio of $\chi'(0)$ or $\chi''_{\max}$ to the case where the ac field is perpendicular to the average magnetization are very close to $\cos^2\theta_M$ and $\sin^2\theta_M$ (0.690 and 0.688 compared to 0.710 for $\theta_h=0°$, 0.312 and 0.313 compared to 0.290 for $\theta_h=90°$; in fact the susceptibility data would be much better reproduced with $\theta_M=56°$). Therefore, except when pumped along the average moment, the thin sample behaves like a macrospin, oriented at θ_M. Its resonance frequency (650 MHz from $\chi'=0$, 603 MHz from the maximum of χ'') corresponds, for an unchanged magnetization, to an anisotropy field $\mu_0 H_{K,\text{eff}}=0.61$ or 0.53 mT. This is much below the anisotropy fields of the two layers (2, respectively, 4 mT), but close to the anisotropy field for the total anisotropy of the sample (0.4 mT), and also close to the apparent saturation field (Fig. 4). This is a clear signature of a nonuniform magnetization state: a macrospin would always show the same resonance frequency.

For the thick sample, the angular region where the spectrum obviously contains several peaks is wider, and a macrospinlike behavior is obtained only when the ac field is perpendicular (to $\pm 50°$) to the average magnetization. The breakdown of the global susceptibility into the modes [Figs. 10(a) and 10(c)] shows that the indices $n=1$, 2, and 3 are involved, whose frequencies are 1145, 1342, and 1696 MHz. It is worthwhile at this point to remark that the two layers, if isolated, would resonate at frequencies $f_1=1174$ MHz and $f_2=1660$ MHz. Therefore, in the limit of large thicknesses, a "double macrospin" model could apply. In order to check this, the computed permeabilities for this double macrospin model are included in the spectra (thin lines labeled 2 MS). As expected, this model predicts only one peak when the ac field is applied along the x and y axes, which is very different from the results of the full model (mostly for an x field, as the average angle is small). The double macrospin model also overestimates the permeability in the parallel orientation and underestimates it in the perpendicular orientation. Both failures are linked to the transition region where the magnetization lies close to the average orientation. Thus, for the double macrospin model to quantitatively apply, still larger thicknesses are needed.

3. Dynamics under a static field

The application of a static field transforms the spiral configuration as shown earlier, by a reduction of the spiral span

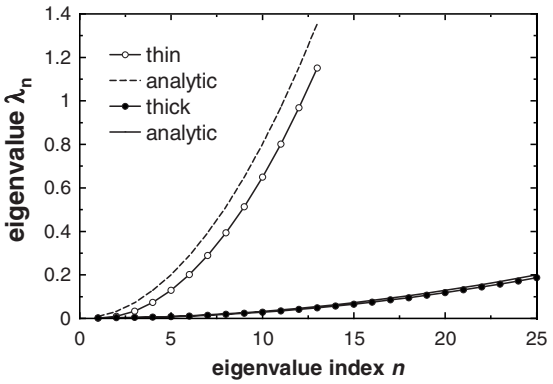

FIG. 8. Variation of the eigenvalues with mode index n, for both sample thicknesses. The curves plot the approximation (31) valid for large n, with $C=4.734\times10^{-4}$ for the thin and $C=1.407\times10^{-3}$ for the thick sample cases, as determined from the potentials plotted in Fig. 2.

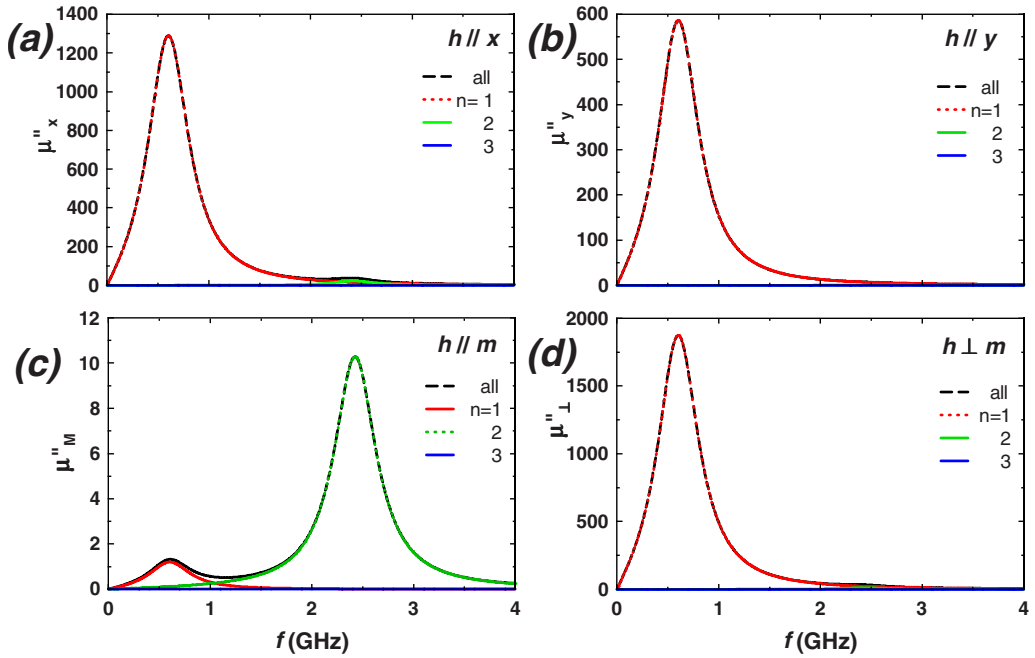

FIG. 9. (Color online) Frequency dependent imaginary part of the permeability calculated for the thin sample, with the contributions from the lowest modes ($n=1$ to 3) shown. The curves labeled "all" were obtained with modes $n=1$ to 13, the last one having a resonance frequency at 26.421 GHz. The ac field orientation is along (a) the x direction: a small contribution from the $n=2$ mode can be seen; (b) the y direction; (c) the angle $\theta_M=57.40°$ of the average magnetization, showing a dominant contribution from the $n=2$ mode; (d) the orthogonal to the average magnetization. Note the greatly varying vertical scales.

and by a change of the average angle of the spiral. The last feature, that is the only one appearing in the case of a macrospin, gives rise to a well known evolution of the resonance frequency. For the two cases considered, the evolution with static field of the resonance frequencies is plotted in Fig. 11. These frequencies were obtained from the calculated spectra by looking for the absolute maximum of the imaginary permeability (even when the spectrum shows several peaks, this

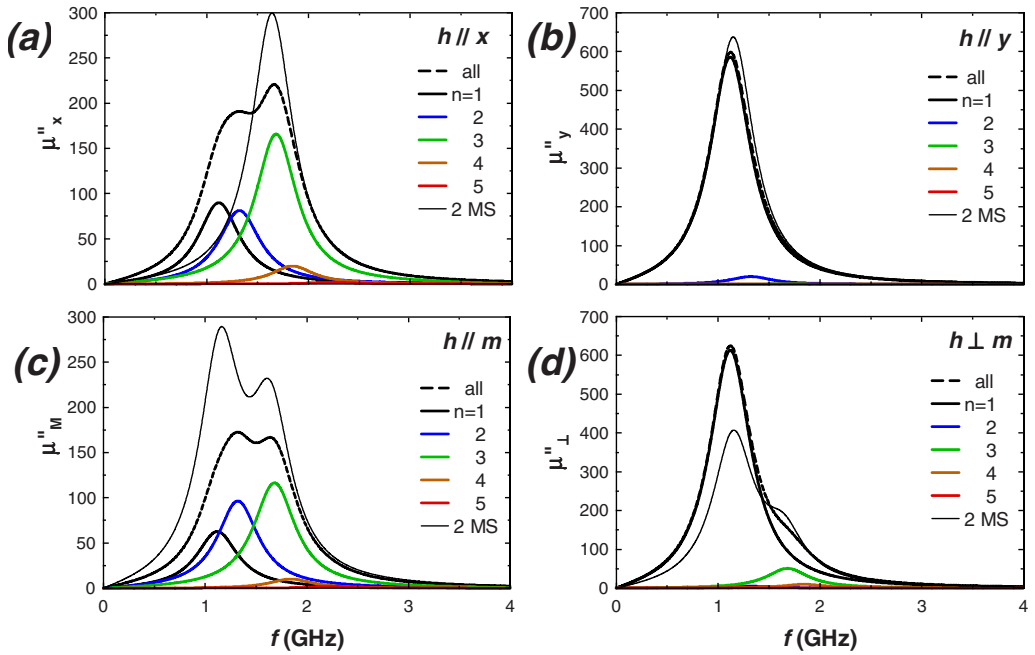

FIG. 10. (Color online) Variation with frequency of the imaginary part of the permeability for the thick sample. The contributions of modes $n=1$ to 5 are also shown. The curve labeled "all" was obtained with modes $n=1$ to 25, the last one having a resonance frequency at 10.658 GHz. Four orientations of the ac field are shown, like in Fig. 9. The thin lines show the results computed in the limit where the two layers are uncoupled (double macrospin model). Note again the different vertical scales of the graphs.

TABLE I. Values of the amplitudes of the low-lying modes in the response of the thin sample to ac fields of various orientations. The eigenvalues and their corresponding frequencies are also given.

ac field		$n=1$	$n=2$	$n=3$	$n=4$	$n=5$
θ_h	λ_n	6.95×10^{-4}	9.70×10^{-3}	3.27×10^{-2}	7.32×10^{-2}	0.129
	f_n (MHz)	649.09	2425.21	4454.57	6663.27	8845.98
0 (x)	h_n/H	0.810	−0.211	0.024	0.005	−0.004
$\pi/2$ (y)	h_n/H	−0.546	−0.035	0.003	0.001	−0.001
θ_M	h_n/H	−0.002	−0.143	0.015	0.003	0.003
$\theta_M+\pi/2$	h_n/H	−0.976	0.159	−0.019	−0.003	−0.003

procedure sorts out the principal absorption). For comparison, the frequency variations with field expected for one or two macrospins are also shown, in the cases where the field is applied along the easy and hard directions.

For the thin sample [Figs. 11(a) and 11(b)], the same frequency is seen whatever the ac field orientation, as it is not applied along the average moment (see Fig. 9). In each case, this frequency changes with applied field similarly to that of a macrospin subjected to a hard axis field, with a zero frequency at $H=H_K$. The values of the corresponding anisotropy fields are $\mu_0 H_K=1.4$ and 0.4 mT, when the field is applied along the x and y axes, respectively. They correspond to the saturation fields of the magnetization curves [see Fig. 4(a)]. This shows that, even if the sample is thin, its dynamic behavior under static field differs from that of a macrospin, that would show a hard axis frequency variation only for one orientation of the field. In addition, for the x orientation of the static field, the frequency starts from a low value and begins to increase, thus mimicking a macrospin magnetized by a field in the easy direction (with $\mu_0 H_K=0.6$ mT here). Such a frequency variation is also absent for a macrospin.

For the thick sample [Figs. 11(c) and 11(d)], the frequencies where absorption is maximum differ for x and y excitations, when the applied field is small. The thin curves drawn correspond here to the two macrospins of the two layers (with the curves expected to be followed for each static field orientation drawn continuous). These curves correspond well to the main peak at low fields, and at higher fields the per-

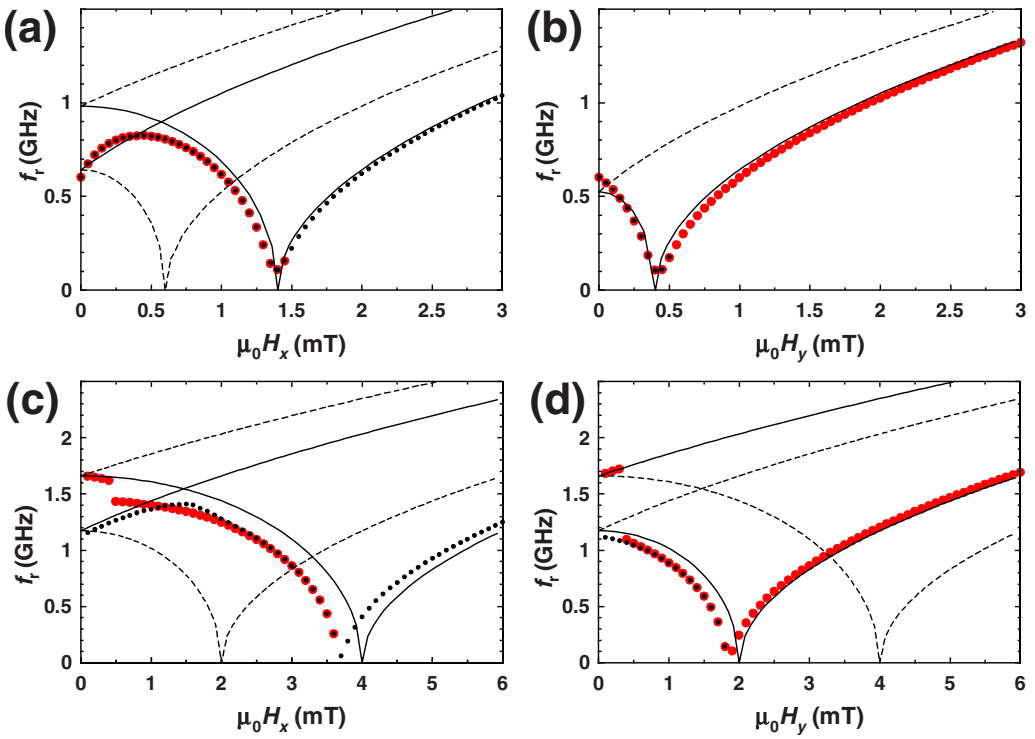

FIG. 11. (Color online) Variation of the resonance frequency (defined as the—single—value where the imaginary permeability is maximum) versus field for the (a,b) thin and (c,d) thick sample. The static field is applied along the (a,c) x axis and the (b,d) y axis. The ac field is, for each panel, applied along the x direction (big red symbols) and along the y direction (small black symbols). The thin curves show the frequencies for macrospins in the zero damping limit, the continuous being those expected to be followed and the dashed those with the static field applied in the other orientation.

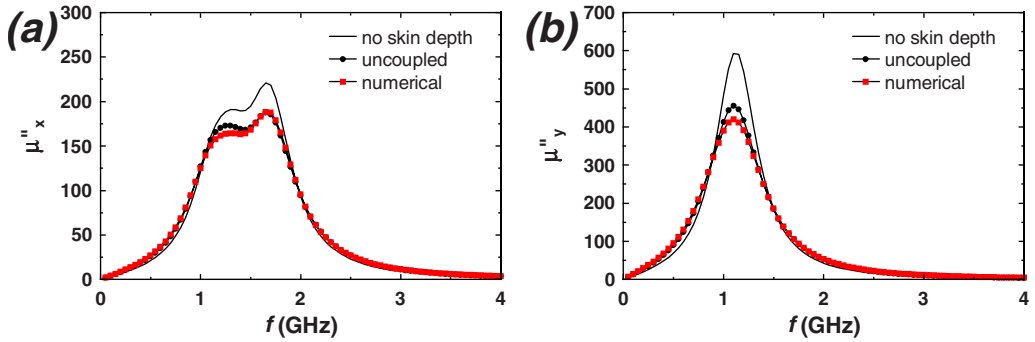

FIG. 12. (Color online) Imaginary part of the permeability for the thick sample, taking into account a resistivity $1/\sigma=1.3\times10^{-6}$ Ω m. The ac field is applied along the (a) x direction and the (b) y direction. The result without skin effect (see Fig. 10, thin line) is compared to the classical skin effect correction [Eq. (33), black circles] and also to the full numerical solution (red squares).

meability of the layer with easy axis normal to the static field dominates. Thus, for a thick sample, the difference with the double macrospin model is mainly apparent on the shape of the permeability spectrum (see Fig. 10).

D. Introduction of the skin effect

For quantitative comparison to experiments, the influence of the skin depth effect cannot be neglected as the samples are not thin compared to the skin depth. In such a case however, the ac magnetic field is no longer uniform across the thickness of the sample. Writing Maxwell's equations in the quasistatic approximation where the propagation wavelength in the sample plane is much larger than the domain size, we get the following equations for the ac fields

$$h_z + m_z = 0,$$

$$\frac{d^2h_y}{dz^2} + \omega^2\varepsilon_0\mu_0\varepsilon(h_y + m_y) = 0,$$

$$\frac{d^2h_x}{dz^2} + \omega^2\varepsilon_0\mu_0\varepsilon(h_x + m_x) = 0. \tag{32}$$

In these formulas, $\varepsilon=1+i\sigma/(\omega\varepsilon_0)$ is the total relative permittivity of the metal with $\varepsilon_r=1$ and including conductivity (σ). The first equation (z components) does not change compared to the previous section, but now the in-plane magnetization and field components are coupled. The coupled system (17) and (32) was solved numerically for a set of the angular frequencies ω in order to compute the permeability spectra.

For the thick sample (Fig. 12), the numerical results are compared to the solution neglecting skin depth effects and, in addition, to the classical calculation where the coupling between Eqs. (17) and (32) is neglected. In the latter case, the apparent permeability μ_a is given as a function of the intrinsic permeability μ_i obtained from Eq. (17) by

$$\mu_a = \mu_i \frac{\tan\left(\frac{\omega}{c}\sqrt{\varepsilon\mu_i}\, t/2\right)}{\frac{\omega}{c}\sqrt{\varepsilon\mu_i}\, t/2}. \tag{33}$$

For the resistivity value chosen (that corresponds to the experimental samples), the spectrum change is mainly a peak broadening with a significant decrease of the amplitude. Most of the change is captured by the classical correction, in agreement with previous results.[14] In this situation at least, no new modes are excited by the inhomogeneous ac field. In the next part, where the 1D spiral model will be compared with experiments, the full skin depth correction will be always applied.

III. EXPERIMENTS

In order to experimentally test the predictions of this model, that we will refer to as 1D spiral model, samples in the form of bilayers with crossed anisotropies were deposited by magnetron sputtering. First, we will describe the experimental details and how the static and dynamic magnetic properties were measured. In a second part, the experimental results will be compared to the 1D spiral model and also to simpler models as the macrospin model or the two (uncoupled) macrospins model.

A. Experimental details

Amorphous ferromagnetic bilayers were deposited by magnetron sputtering from a CoNb target. The base pressure before the deposition was less than 5×10^{-6} mbar. During the process, the pressure was maintained at 5×10^{-3} mbar and the sputtering power at 14 W/cm^2. The bilayers were grown using an *in situ* rotatable sample holder. A first layer with nominal thickness $t_1=250$ nm was deposited on a glass square substrate of 9 mm width whose the uniaxial magnetic anisotropy in the film plane is induced by the residual magnetron field. With the sputtering still taking place, the sample was then rotated by $\pi/2$ in a few milliseconds, leading to the growth of the second layer. In this way, the magnetic anisotropies are expected to be perpendicular to each other so that a bilayer with crossed anisotropies is produced. Moreover, as the growth was not interrupted, the exchange coupling between the two layers should be intact. As the deposition time is the same for each layer, the thickness of the top layer is expected to be equal to the thickness of the first. The whole thickness of the bilayer ($t=500$ nm) was

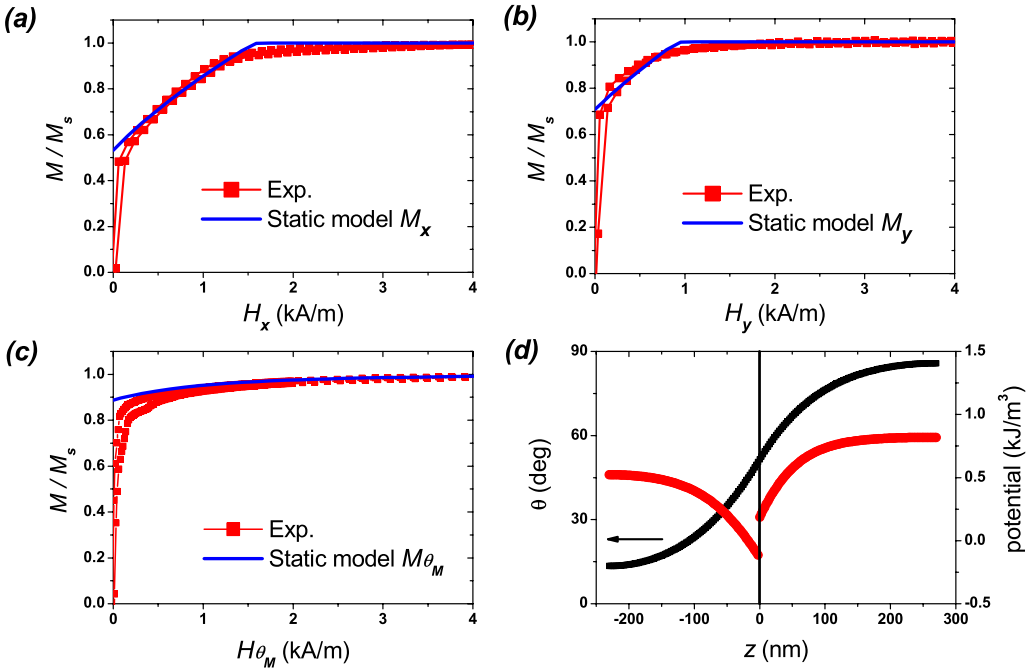

FIG. 13. (Color online) Experimental magnetization curves of the bilayer with crossed anisotropies along the (a) x, (b) y axes and at (c) 45°. Blue curves, corresponding to the magnetization curves computed with 1D spiral model described in Sec. II B with the parameters given in Sec. III B, are superposed to the data. For (c), the calculation was performed for a static field along the average magnetization, corresponding to an angle θ_M=53.16°. Panel (d) plots the computed profile of the magnetization angle of for this bilayer (the dynamic potential is also drawn).

measured using a Dektak profilometer. Due to the amorphous nature of the material (checked by x-ray diffraction), the value of the electrical resistivity measured with a four-probe method is rather large (about 1.4 $\mu\Omega$. m) in accordance to prior results.[23] Thus, the skin depth effect should be taken into account for the calculation of the permeability.

Regarding static magnetic properties, the saturation magnetization M_s and the anisotropy fields were determined from the hysteresis loops at room temperature measured with a standard vibrating sample magnetometer. High frequency permeability spectra from 100 MHz to 6 GHz were measured with a permeameter based on a single coil device,[24,25] under a static magnetic field H_0 up to 12 kA/m (150 Oe). This field can be applied either parallel or perpendicular to the dynamic field h of the single coil, and the square sample can be positioned with its x axis or y axis along the dynamic field. Therefore, in the following, the measurement configurations will be referred to as (H_x,h_x), (H_x,h_y), etc. We define μ_i' as the real part of the permeability at 100 MHz and $\mu''_{\max}$ as the maximum value of the imaginary part of the permeability. From the permeability spectra, the resonance frequency f_r was defined as the frequency where either the real permeability is equal to 1 ($\mu'=1$), or where the imaginary part μ'' is maximum. Although several thicknesses of the two layers were fabricated, only the nominally symmetric bilayer will be presented, as it is the most significant sample.

B. Static magnetic properties

Several normalized magnetization curves of the bilayer are shown in Fig. 13. The static field H_0 is applied along the x (a) and y (b) axes corresponding to the easy axis of the first and second layer, respectively. First, the saturation magnetization of the sample is found to be 690 ± 35 kA/m whereas the coercivity is weak ($H_c \sim 80$ A/m). Second, we can observe that the magnetization curves show a shape that is different from the typical one for samples with uniaxial magnetic anisotropy, where the fast change of the magnetization at low applied fields is attributed to wall displacements. The magnetization values at the remanence M_r for each curves differ, indicating that the bilayer is slightly dissymmetric. It is worth noting that the two layers may present different magnetic properties because their growth takes place on different substrates (glass and metal, respectively). From such hysteresis loops, no suitable anisotropy fields but only saturation fields can be accurately estimated. The magnetization curves generated from the numerical solution of the 1D spiral model detailed in Sec. II B 2 are superposed to the data.

The appropriate numerical values, taken for all static and dynamic simulations of this sample, differ a little from those of the first part and read: M_s=690 kA/m, $A=0.7 \times 10^{-11}$ J/m, H_{K1}=1.3 kA/m (17 Oe), H_{K2}=1.9 kA/m (24 Oe), t_1=230 nm, t_2=270 nm, and α=0.016. The figure shows that the model is able to generate a realistic description of the magnetization rotation in the nonuniform state, regarding the remanence and the saturation field. The marked curvature of the magnetization curves, not reproduced by the model, should be investigated in more details (it is attributed to dispersion of anisotropy or field misalignment). Obviously, the coercivity related to wall displacements cannot be described within this model that neglects any in-plane variation of magnetization.

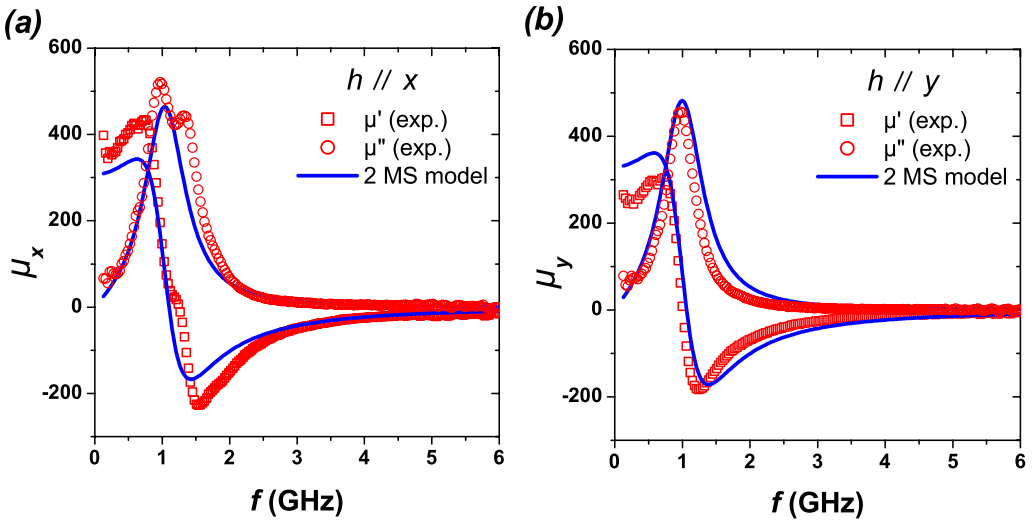

FIG. 14. (Color online) Real and imaginary parts of the permeability as a function of the frequency measured along the x (left) and y (right) directions (red symbols). The thin blue curves show the fit of the data by the double macrospin model.

In order to illustrate the expected depth dependence of the magnetization orientation, the corresponding calculated $\theta(z)$ profile and the potential calculated from the zero field static model are plotted in Fig. 13(d). The end values $\theta_1=13.45°$ and $\theta_2=85.69°$ are a little away from the easy axes, as the thicknesses are moderately larger than the characteristic lengths $\Delta_i: t_1/\Delta_1=2.11$ and $t_2/\Delta_2=2.94$. The angle of the average magnetization is $\theta_M=53°$. As the average magnetization of the sample is oriented at roughly $\pi/4$ from the axes, another hysteresis loop measured along this direction is displayed in Fig. 13(c). The remanence is close to 1 and the agreement with the model rather good in the magnetization rotation region.

C. Dynamic magnetic properties

In addition to the magnetization measurements under static fields, high frequency permeability measurements under a static field were performed, and will be compared to the results of the 1D spiral model. The four configurations of both fields mentioned earlier should all be explored as the two layers of the sample are different.

1. Zero field case

Figure 14 displays the permeability spectra from 100 MHz to 6 GHz, with no applied field. Large permeability levels are measured along x (h_x) and y (h_y) axes, which are mainly related to the response of the second layer and the first layer, respectively. The resonance frequencies f_r along both axes, when defined by $\mu'(f_r)=1$, differ by 17%. This is related to the existence of two resonance peaks under h_x excitation. On the contrary, the alternative definition through the maximum of $\mu''(f)$ gives the same values ($f_r \approx 1$ GHz). It appears that the determination of f_r for the sample considered here is more complex than for a single layer with uniaxial magnetic anisotropy, since the permeability spectra show several resonance peaks. Therefore, we will from now define f_r by the maximum of μ''. Note that, for a monolayer with $t=500$ nm and the same conditions of deposition, the measured f_r value is distinctly higher, close to 1.2 GHz.

A simple treatment of the data of Fig. 14 is to try to fit them with a double macrospin model discussed above, i.e., assuming that the two layers are uncoupled and therefore respond each as a macrospin. With the parameters $M_s=725$ kA/m $(\mu_0 M_s=0.91$ T), $H_{K1}=1100$ A/m, $H_{K2}=700$ A/m, and $\alpha=0.019$, the thin curves superposed to the data are obtained. The value of the damping thus obtained is slightly large, the saturation magnetization is found larger than the VSM value and the two peaks seen for the h_x excitation are evidently not reproduced, so that such a model is not satisfactory. The comparison to the 1D spiral model will be presented in the next section, when the spectra under field are discussed.

2. Nonzero field

The measured frequency-dependent permeability is displayed in Fig. 15 as a function of static field for the two main configurations (H_x,h_y) and (H_y,h_x). Especially, the splitting of the resonance peak for the (H_x,h_y) case under field is related to the dynamic response tailored by both K_1 and K_2, whereas this splitting is visible even without applied field for the (H_y,h_x) case. The simulated permeability spectra for the lower fields show a slight shift in frequency compared to the experimental permeability whereas, for the two higher fields, the model agrees fairly well with the measured permeability peak positions. The agreement is extremely good in the (H_y,h_x) case, corroborating what was already seen on the magnetization curves (Fig. 13). In both cases, it is remarkable that, even if the applied fields are much above the apparent saturation fields (1500 A/m for H_x, 1000 A/m for H_y), the spectra still show two clear peaks, a feature well reproduced by the 1D spiral model.

In order to be more quantitative, the two main characteristics of the spectra will be studied, namely, the square resonance frequency f_r^2 and the value of the maximum imaginary permeability $\mu''_{\max}$. Figure 16 displays the measured f_r^2 as a

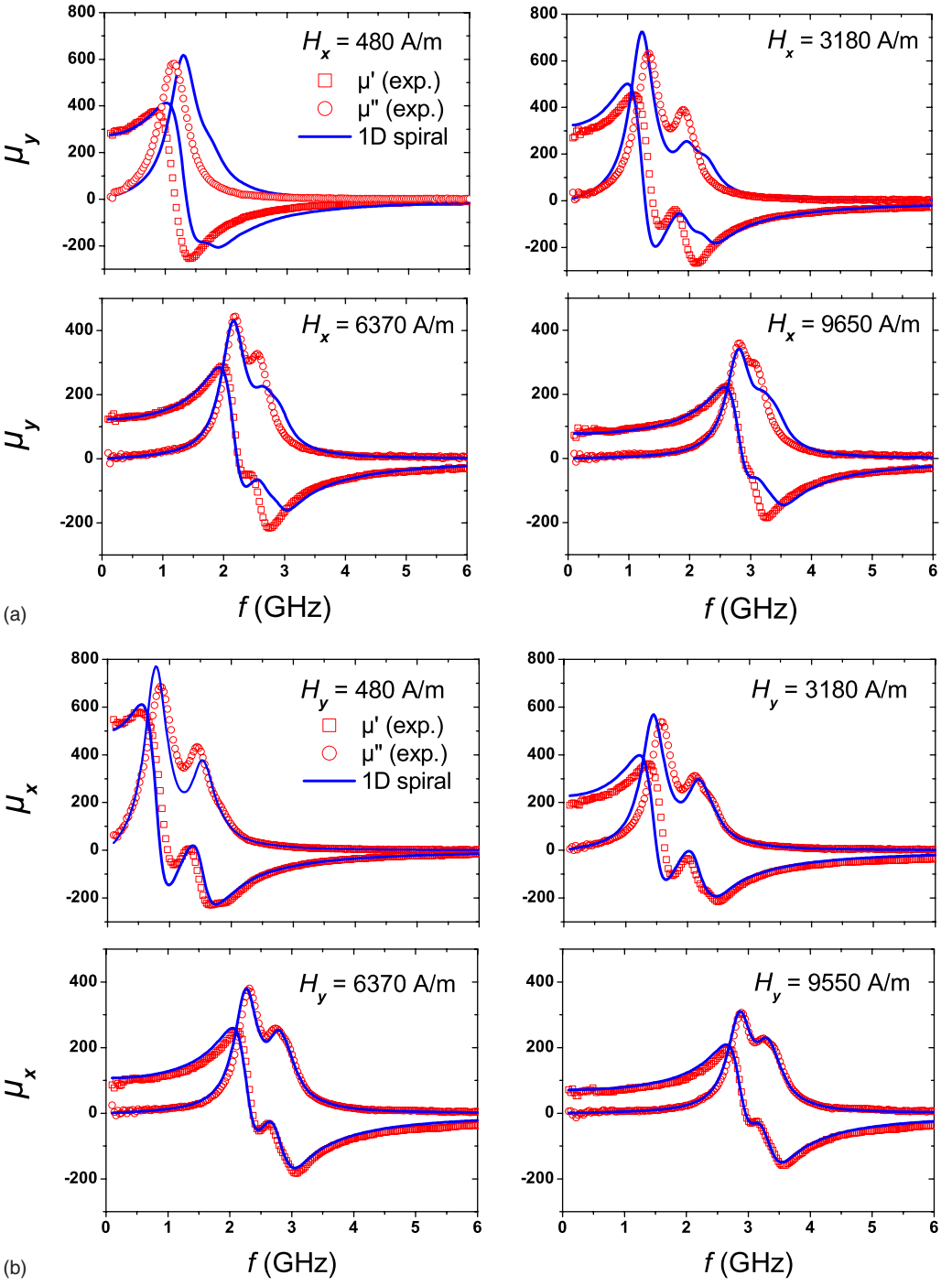

FIG. 15. (Color online) Measured permeability spectra (red symbols), under several static fields and for the 'standard' configurations (a) (H_x,h_y) and (b) (H_y,h_x). The results of the 1D spiral model are shown by the blue lines.

function of the static field applied up to 12 kA/m (150 Oe) for the two configurations (H_x,h_y) and (H_y,h_x). As the spectra show two well separated peaks, the values will be given for each. In the case (H_x,h_y), the complex behavior of the square resonance frequency of the first peak is striking compared to what is expected for a macrospin. However, such a behavior was already seen in Fig. 11, and the 1D spiral model reproduces well the experiment.

In the case of a macrospin, the f_r^2 dependence is described by the Kittel's equations,[2] for a field $H > H_K$ oriented in the plane, either perpendicular or parallel to the easy axis (see also Fig. 11)

$$f_{r\perp}^2 = \left(\frac{\gamma_0}{2\pi}\right)^2 [M_s . (H - H_K)], \tag{34}$$

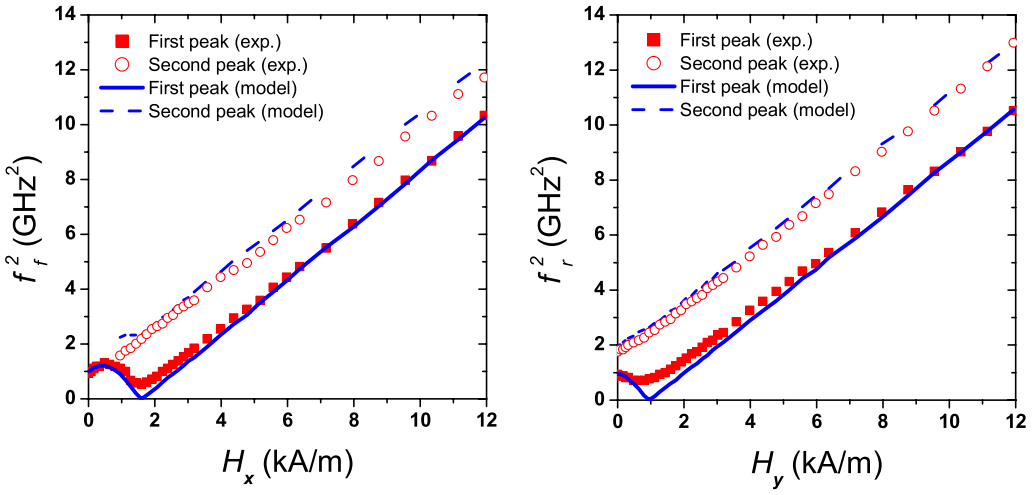

FIG. 16. (Color online) Applied field dependence of the square resonance frequency (red symbols) for the standard configurations where dc and ac fields are orthogonal (H_x,h_y) (left) and H_y,h_x (right). The dependence of f_r^2 is linear at higher field, as well known. Resonance frequencies (blue lines) were calculated from the 1D spiral model with the parameters given in Sec. III B.

$$f_{r\|}^2 = \left(\frac{\gamma_0}{2\pi}\right)^2 [M_s . (H + H_K)]. \tag{35}$$

Effective dynamic anisotropy fields H_{K1} and H_{K2} can thus be obtained as intercepts of the linear fits to $f_r^2=0$. From the data, we get $H_{K1,\|}=770$ A/m (9.7 Oe) and $H_{K2,\perp}=1240$ A/m (15.6 Oe) for the case (H_x,h_y), and $H_{K1,\perp}=420$ A/m (5.3 Oe) and $H_{K2,\|}=1650$ A/m (20.7 Oe) for the case (H_y,h_x). For a perfect uniaxial anisotropy layer, the linear extrapolations should cross the H axis at the same values $(H_{K,\|}=H_{K,\perp})$, but here a strong difference between the two values is observed. This is commonly attributed to magnetization dispersion,[26] which is verified here as the dispersion was indeed created in the sample. The estimated anisotropy fields, empirically derived from the average of $H_{K,\|}$ and $H_{K,\perp}$ calculated either from the linear relations or from the extrapolations to the applied field axis, are $H_{K1}=595$ A/m and $H_{K2}=1445$ A/m. Nevertheless, it is impossible to describe the f_r^2 dependence for the configurations (H_x,h_y) and (H_y,h_x) with the same set of values of H_{K_1} and H_{K_2}.

On the other hand, the numerical results using the 1D spiral model with full treatment of the exchange interaction are also plotted in Fig. 16, and agree very well with the applied field dependence of the experimental f_r^2. We remark that the anisotropy fields $(H_{K1}=1.3$ kA/m and $H_{K2}=1.9$ kA/m) used for the simulation are larger than all those deduced previously from the linear f_r^2 dependence. To generate the dynamic response, the skin effect calculation (with $\rho=1.4$ $\mu\Omega.m$ as deduced from electrical measurements) was carried out on the basis of the relations detailed in Sec. II D. The magnetic damping parameter α used is smaller than that obtained by fitting the zero field results with the permeability of a single macrospin. The model describes perfectly the emergence of the second peak for the configuration (H_x,h_y) and the singular behavior associated to the first peak for $H<1.6$ kA/m. However, the drop of the resonance frequency, associated with the first peak behavior around the anisotropy field H_{K1} is overestimated in the model. This fact is also attributed to anisotropy dispersion or field misalignment.

Experimental and numerical permeability maximum values, as a function of the static field are plotted in Fig. 17. The overall agreement is good, but one may notice that the permeability associated with the first peak, for a field $H\approx H_{K2}=1.9$ kA/m, is overestimated. This feature results directly from what was seen on the square resonance frequency. Second, the model predicts systematically an underestimated value for the second peak, but this again occurs for the (H_x,h_y) configuration.

The comparison between the experimental and calculated permeability was also performed for the two nonstandard configurations where dc and ac fields are parallel, namely, (H_x,h_x) and (H_y,h_y). The static field values were chosen from the magnetization curves shown in Fig. 13. The spectra (Fig. 18) show the expected rapid decrease of permeability as the field increases (beware that fields are much smaller than in Fig. 15), due to the fact that the susceptibility is measured parallel to the static field. The agreement between 1D spiral model and experiments is good for low fields, but deteriorates close to the computed saturation. This however reflects the disagreement already seen on the magnetization curves.

IV. CONCLUSION

In this paper, we have studied in detail the statics and dynamics of a model sample with nonuniform magnetic structure, namely, a bilayer with crossed anisotropies. For statics, we have established a general analytic solution that predicts the magnetic profile, in zero field and under applied field, from the key parameters of the system (the reduced thicknesses, the anisotropy ratio, the reduced fields). For the linear dynamics under infinitesimal ac field, we have shown that the low-lying modes are close to eigenmodes of a relevant Schrödinger equation, with a potential that derives from the static magnetization profile. These modes provide a direct interpretation of the permeability spectra, and allow

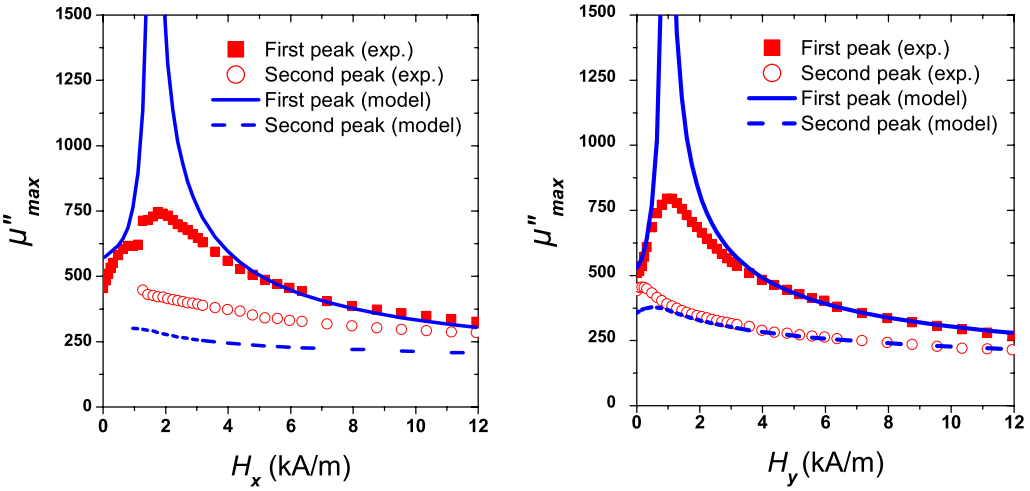

FIG. 17. (Color online) Maximum permeability $\mu''_{\max}$ (red symbols) as a function of the static field applied for two standard configurations of the fields: (H_x,h_y) (left) and (H_y,h_x) (right). The calculated values with the 1D spiral model (same parameters as for Fig. 16) are drawn by the blue lines.

generalizing a sum rule on the permeability previously derived in the macrospin approximation (see Appendix). This analytic framework is however limited to insulating samples. For conductive samples, a full numerical solution was constructed and compared to this analytic limit, with minor deviations for the parameters that were used.

In the second part of the paper, this 1D spiral model has been compared to experiments performed on soft samples designed to be of bilayer structure with crossed anisotropies. For this, static and dynamic measurements have been made. We have obtained good overall agreement with a single set of thicknesses and anisotropies, qualitatively and quantitatively (some systematic deviations appear, attributed to misalignment between the easy axes and the sample edges). Thus, we conclude that the nonmacrospin behavior often seen in static and dynamic measurements of such soft and thick samples can be attributed to structures that are inhomogeneous in the thickness.

The next step on this path could be to invert the approach: starting from static and dynamic measurements, to find the anisotropy distribution across the sample thickness.

APPENDIX: SUM RULES ON THE MAGNETIZATION DYNAMICS FOR A 1D NONUNIFORM MAGNETIZATION

From the permeability spectra of soft thin films, a dynamically coupled magnetization M_μ with components $M_{\mu,x}$ and $M_{\mu,y}$ has been defined[21] as

$$M_{\mu,x}(F) = \frac{2\pi}{\gamma_0}\sqrt{\frac{2}{\pi}\int_0^F \mu''_x(f)\,.\,f\,.\,df}, \tag{36}$$

(and similarly for the y permeability), with $M_\mu = \sqrt{M_{\mu,x}^2 + M_{\mu,y}^2}$. In addition, a sum rule has been introduced, stating that, for $F=\infty$, M_μ is equal to the saturation magnetization M_s. At the root of the sum rule lies the identification of the dynamically coupled magnetizations to r.m.s. magnetizations according to

$$M_{\mu,x} = M_s\sqrt{\langle m_y^2\rangle}, \tag{37}$$

and similarly for the y permeability (the average $\langle\ \rangle$ is over space).

These relations were first derived[21] in the case of a collection of macrospins that may interact magnetostatically but not by exchange. Recently, estimates of the corrections to apply to M_μ in order to remove the effect of a finite F, or of the skin effect, were proposed,[27] that widen the applicability of this analysis. Moreover, the sum rule has been observed to hold in more complex situations where the magnetization is not uniform, such as bilayers similar to those considered here.[15] For example, from the spectra shown in Fig. 14, without corrections and for $F=6$ GHz, we obtain $M_{\mu,x}=547$ and $M_{\mu,y}=394$ kA/m, leading to $M_\mu=673$ kA/m. This value, close to the VSM value of M_s, becomes still closer (691 kA/m) with the corrections.

Therefore, an investigation of the validity of the sum rule for a continuous but nonuniform magnetization, where exchange plays an important role, would be desirable. In this section, using the expression of the susceptibility without skin effect as a sum over modes, we will prove that the sum rule holds.

The in-plane rf magnetization comes from the variation of the angle θ and reads

$$\vec{m}_{\rm rf}(z) = M_s\Sigma_n a_n U_n(z)[-\sin\,\theta_0(z), \cos\,\theta_0(z), 0]. \tag{38}$$

In order to get the susceptibility without skin depth effects, this magnetization has to be projected along the ac field, and averaged over z. Thus, the susceptibility for an a.c. field applied at an in-plane angle θ_h reads

$$\chi = \frac{\cos\,\theta_h\int m_x + \sin\,\theta_h\int m_y}{(t_1+t_2)H}$$

$$= -\frac{M_s}{(t_1+t_2)H}\Sigma_n a_n\int U_n(z)\sin[\theta_0(z)-\theta_h]dz. \tag{39}$$

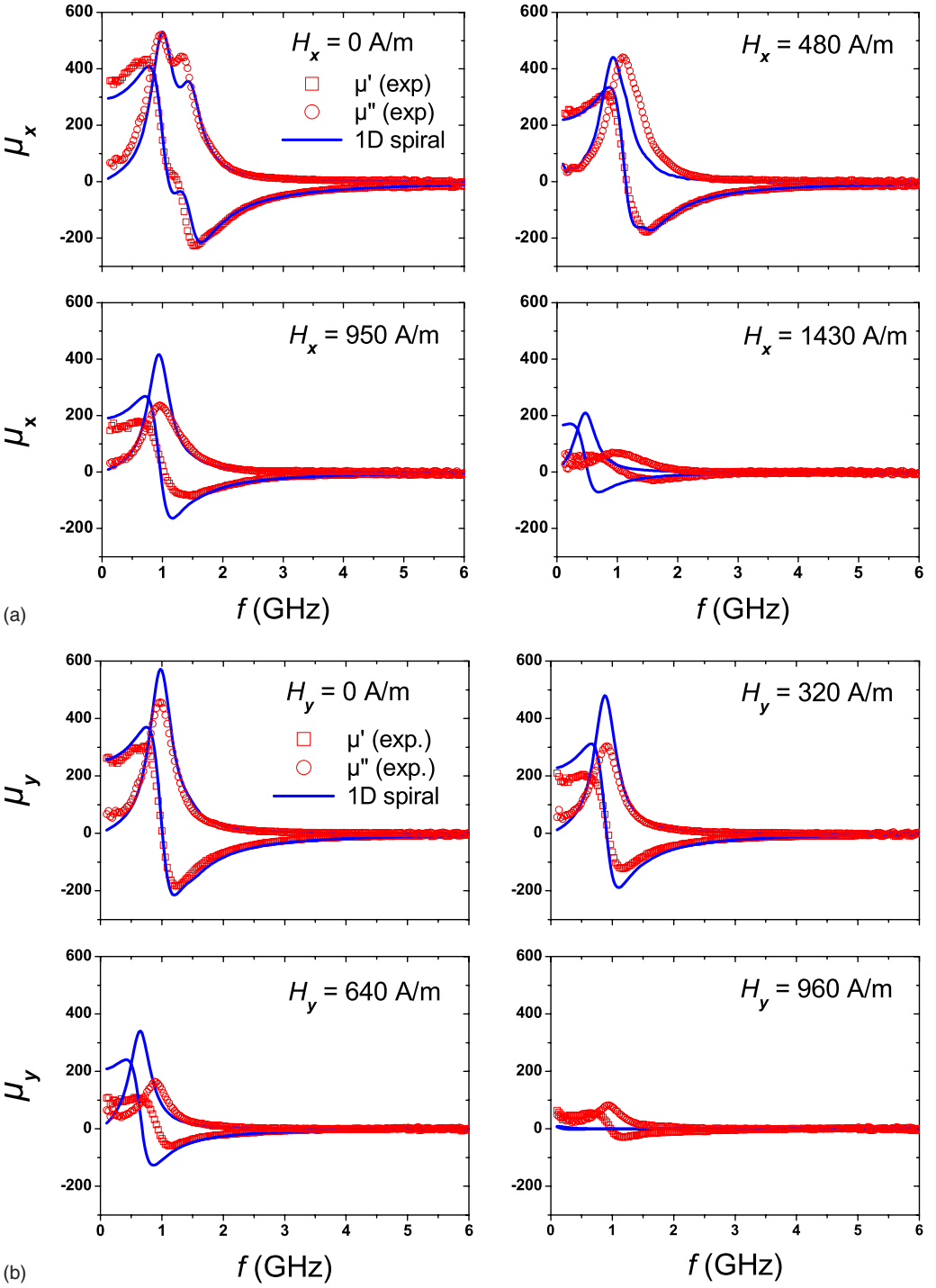

FIG. 18. (Color online) Measured permeability spectra (red symbols), under several static fields and for the "nonstandard" configurations (a) (H_x,h_x) and (b) (H_y,h_y). The results of the 1D spiral model are shown by the blue lines. Note, for zero field, the better match of the data with the 1D spiral than with the two macrospins model shown in Fig. 14.

The demonstration of the sum rule rests on the evaluation of the integral by contour integration in the complex frequency plane.[21] As a result, the integral of imaginary permeability times frequency is proportional to the limit at $\omega \to \infty$ of the product $\omega^2\chi$, neglecting the Gilbert damping term that causes the integral to diverge.[27] From the expression (29) of χ we get here

$$\omega^2\chi \to (\gamma_0 M_s)^2 \Sigma_n \frac{\left[\int U_n(z)\sin(\theta_0-\theta_h)dz\right]^2}{(t_1+t_2)^2}. \quad (40)$$

By developing $\sin(\theta_0-\theta_h)$ on the U_n basis and evaluating its norm, we also have

$$\int \sin^2(\theta_0 - \theta_h)dz = \frac{1}{t_1 + t_2}\Sigma_n \left[\int U_n \sin(\theta_0 - \theta_h)dz\right]^2. \tag{41}$$

Thus, the limit of $\omega^2\chi$ can be rewritten as

$$\omega^2\chi \to \frac{(\gamma_0 M_s)^2}{t_1 + t_2}\int \sin(\theta_0 - \theta_h)^2. \tag{42}$$

Applying the ac field in the orthogonal direction amounts to changing θ_h into $\theta_h + \pi/2$. Therefore, the sum of the limits for two orthogonal field directions (denoted by 1 and 2) is simply

$$\omega^2(\chi_1 + \chi_2) \to (\gamma_0 M_s)^2. \tag{43}$$

This completes the proof of the sum rule (or, equivalently, of the properties of the dynamically coupled magnetization) in a situation where exchange plays an important role. The calculation has shown that several assumptions underlie this proof: (i) weak anisotropy field that allows a direct solution for the ac magnetization in the direction normal to the film plane; (ii) low frequencies ($\omega \ll \gamma_0 M_s$) and (iii) absence of skin effect (see Ref. 27 for a discussion of this point). The final result is not so surprising once it is realized that the permeability is decomposed on orthogonal modes, each contributing with a one macrospin form.

[1] L. Landau and E. Lifshitz, Phys. Z. Sowjetunion **8**, 153 (1935).
[2] C. Kittel, Phys. Rev. **73**, 155 (1948).
[3] *Spin Dynamics in Confined Magnetic Structures I, Topics in Applied Physics*, edited by B. Hillebrands and K. Ounadjela (Springer Verlag, Berlin, 2002), Vol. 83.
[4] *Spin Dynamics in Confined Magnetic Structures II, Topics in Applied Physics*, edited by B. Hillebrands and K. Ounadjela (Springer Verlag, Berlin, 2003), Vol. 87.
[5] *Spin Dynamics in Confined Magnetic Structures III, Topics in Applied Physics*, edited by B. Hillebrands and A. Thiaville (Springer Verlag, Berlin, 2006), Vol. 101.
[6] L. He, W. Doyle, and H. Fujiwara, IEEE Trans. Magn. **30**, 4086 (1994).
[7] C. Serpico, I. Mayergoyz, and G. Bertotti, J. Appl. Phys. **93**, 6909 (2003).
[8] T. Devolder, H. Schumacher, and C. Chappert, *Spin Dynamics in Confined Magnetic Structures III* (Springer, Berlin, 2006), pp. 1–56.
[9] G. Bertotti, C. Serpico, I. D. Mayergoyz, A. Magni, M. d'Aquino, and R. Bonin, Phys. Rev. Lett. **94**, 127206 (2005).
[10] R. D. McMichael, D. J. Twisselmann, and A. Kunz, Phys. Rev. Lett. **90**, 227601 (2003).
[11] A. Hubert and R. Schäfer, *Magnetic Domains* (Springer Verlag, Berlin, 1998).
[12] C. Bayer, J. Jorzick, S. Demokritov, A. Slavin, K. Guslienko, D. Berkov, N. Gorn, M. Kostylev, and B. Hillebrands, *Spin Dynamics in Confined Magnetic Structures III* (Springer, Berlin, 2006), pp. 57–104.
[13] D. Lee and S. Wang, J. Appl. Phys. **99**, 08F109 (2006).
[14] O. Acher, S. Dubourg, F. Duverger, and N. Malléjac, J. Magn. Magn. Mater. **310**, 2319 (2007).
[15] O. Acher, V. Dubuget, and S. Dubourg, IEEE Trans. Magn. **44**, 2842 (2008).
[16] N. Vukadinovic, O. Vacus, M. Labrune, O. Acher, and D. Pain, Phys. Rev. Lett. **85**, 2817 (2000).
[17] J. Ben Youssef, N. Vukadinovic, D. Billet, and M. Labrune, Phys. Rev. B **69**, 174402 (2004).
[18] F. Schoenstein, P. Aublanc, H. Pagès, S. Queste, V. Barentin, A. Adenot, N. Malléjac, and O. Acher, J. Magn. Magn. Mater. **292**, 201 (2005).
[19] E. Goto, N. Hayashi, T. Miyashita, and K. Nakagawa, J. Appl. Phys. **36**, 2951 (1965).
[20] L. M. Álvarez-Prado, S. M. Valvidares, J. I. Martín, and J. M. Alameda, Phys. Rev. B **76**, 214419 (2007).
[21] O. Acher and A.-L. Adenot, Phys. Rev. B **62**, 11324 (2000).
[22] A. Thiaville and A. Fert, J. Magn. Magn. Mater. **113**, 161 (1992).
[23] S. Otomo, J. Mater. Sci. **31**, 3805 (1996).
[24] D. Pain, M. Ledieu, O. Acher, A.-L. Adenot, and F. Duverger, J. Appl. Phys. **85**, 5151 (1999).
[25] J. Peuzin and J. Gay, *Acte Des Journées D'études Sur La Caractérisation Microonde Des Matériaux Absorbants* (unpublished, 1991), p. 75.
[26] K. Kempter and H. Hoffmann, Phys. Status Solidi **34**, 237 (1969).
[27] O. Acher and S. Dubourg, Phys. Rev. B **77**, 104440 (2008).